IEEE Access
Multidisciplinary | Rapid Review | Open Access Journal

Received February 28, 2021, accepted April 22, 2021, date of publication May 7, 2021, date of current version May 19, 2021.

Digital Object Identifier 10.1109/ACCESS.2021.3078410

The Frequency- and the Time-Domain Design of a Dual Active Bridge Converter Output Voltage Regulator Based on the $\mathfrak{D}$-Decomposition Technique

KAROL NAJDEK AND RADOSLAW NALEPA
Department Electrical Power Engineering, Wrocław University of Science and Technology, 50-370 Wrocław, Poland
Corresponding author: Radoslaw Nalepa (radoslaw.nalepa@pwr.edu.pl)

ABSTRACT Commonly used variants of the proportional-integral, PI, and the integral-proportional, IP, compensator gains selections, merged with the $\mathfrak{D}$-decomposition technique are presented in this paper. The motivation to this work is the willingness to check whether such a combination can lead to unified and perhaps simplified approach in this matter. Therefore, the $\mathfrak{D}$-decomposition technique has been effectively combined with the frequency- and the time-domain driven requirements regarding the control dynamics. Criteria such as the gain- and phase-margins, (GM, PM), the sensitivity, M_S, the pole placements by means of the (σ, ω_d) and the (ξ, ω_n), and the overshoot with the rise time (δ, t_r) are considered. It has been shown that the control design effort can be reduced by the means of the $\mathfrak{D}$-decomposition to intuitive judgments in the proportional and integral gains coordinates (K_P, K_I) with parametric curves. As such it can be thought of as a promising scenario in a case considered. The analyses are presented and discussed in details. They are conducted basing on example of output voltage closed loop control of the Dual Active Bridge, DAB, converter. The circuit operates under the phase shift control scheme. The control-to-output transfer function identification and the control circuit delays are included in the analyses. The case analysis have shown that the time domain requirements are less effectively met with the PI regulator when compared to its IP configuration. This is due to the commonly used simplifications during conversion between the (ξ, ω_n) and the (δ, t_r) in presence of uncompensated zero of the closed loop transfer function. The paper contains complete and intelligible approach to dedicated mathematical investigations verified experimentally.

INDEX TERMS Controller design, $\mathfrak{D}$-decomposition technique, Dual Active Bridge converter, frequency domain constraints, frequency response analysis, gain margin, phase margin, pole placement, sensitivity, time domain constraints, transfer function identification.

NOMENCLATURE

A2D	- Analog-to-Digital
DAB	- Dual Active Bridge converter
PWM	- Pulse Width Modulation
GM	- Gain Margin
PM	- Phase Margin
ω	- pulsation
ω_d	- imaginary part of the complex Laplace operator, - damped natural pulsation,
ω_n	- undamped natural pulsation
σ	- real part of the complex Laplace operator
ξ	- damping ratio
$\Delta\mathfrak{D}_0$	- $(m-1)-$dimentional hyperplane where a real zero of the characteristic equation is located at the origin of the $s-$plain
δ	- overshoot in general
δ^{dem}	- overshoot measured demand
$\delta^{sim,m}$	- overshoot measured in simulation
$\delta^{exp,m}$	- overshoot measured in experiment
η_{DAB}	- DAB assumed efficiency
$\Phi^{ref}_{DAB,out}$	- DAB output side phase shift reference
τ_{A2D}	- A2D driven time-delay
τ_{PWM}	- PWM driven time-delay

The associate editor coordinating the review of this manuscript and approving it for publication was Huiping Li.

$\tilde{\varphi}^{\mathrm{ref}}_{\mathrm{DAB,out}}$ - DAB output side phase shift reference perturbation
$\varphi_{\mathrm{DAB,in}}$ - DAB input side phase shift
$\varphi_{\mathrm{DAB,out}}$ - DAB output side phase shift
$a_{\mathrm{M_S}}$ - real part of a complex number for desired M_{S}
a_{GM} - real part of a complex number for desired GM
a_{PM} - real part of a complex number for desired PM
$b_{\mathrm{M_S}}$ - imaginary part of a complex number for desired M_{S}
b_{GM} - imaginary part of a complex number for desired GM
b_{PM} imaginary part of a complex number for desired PM
$C(s)$ - controller transfer function
$C_{\mathrm{DAB,in}}$ - DAB input capacitance
$C_{\mathrm{DAB,out}}$ - DAB output capacitance
$D_{\mathrm{DAB,in}}$ - duty cycle, DAB input side
$D_{\mathrm{DAB,out}}$ - duty cycle, DAB output side
$E(s)$ - error
f_{s} - switching frequency
$G_{\mathrm{CL}}(s)$ - close-loop transfer function
$G_{\mathrm{OL}}(s)$ - open-loop transfer function
$i_{\mathrm{DAB,in}}$ - DAB input current
$i_{\mathrm{DAB,out}}$ - DAB output current
i_{L} - inductor current
$i_{\mathrm{T,in}}$ - transformer input current
K - plant gain
K_{I} - PI regulator integral gain
K_{P} -PI regulator proportional gain
n - transformer turns ratio
$N_{\mathrm{T,in}}$ - number of transformer input side turns
$N_{\mathrm{T,out}}$ - number of transformer output side turns
$P(s)$ - plant transfer function
$P^{\mathrm{exp,est,c2o}}_{\mathrm{DAB}}(s)$ - DAB control-to-output estimated transfer function, from experimentally measured points
$P^{\mathrm{rtd}}_{\mathrm{DAB}}$ - DAB rated power
$R(s)$ - reference signal
T_{dt} - gate drive signal dead time
T_{o} - plant time constant
t_{r} - rise time
$t^{\mathrm{exp,m}}_{\mathrm{r}}$ - rise time measured in experiment
$t^{\mathrm{sim,m}}_{\mathrm{r}}$ - rise time measured in simulation
$U(s)$ - control signal
$v_{\mathrm{DAB,in}}$ - DAB input voltage
$V^{\mathrm{rtd}}_{\mathrm{DAB,in}}$ - DAB rated input voltage
$v_{\mathrm{DAB,out}}$ - DAB output voltage
$v^{\mathrm{exp,m,c2o}}_{\mathrm{DAB,out}}$ - DAB output voltage measured in experiment as response to $\varphi_{\mathrm{DAB,out}}$ variation during identification of the control to output transfer function
$v^{\mathrm{exp,m}}_{\mathrm{DAB,out}}$ - DAB output voltage measured in experiment
$v^{\mathrm{mat,c}}_{\mathrm{DAB,out}}$ - DAB output voltage calculated in mathematical model
$v^{\mathrm{m}}_{\mathrm{DAB,out}}$ - DAB output voltage measured in general
$V^{\mathrm{ref}}_{\mathrm{DAB,out}}$ - DAB output voltage reference
$V^{\mathrm{rtd}}_{\mathrm{DAB,out}}$ - DAB rated output voltage
$v^{\mathrm{sim,m}}_{\mathrm{DAB,out}}$ - DAB output voltage measured in simulation
v_{L} - voltage across the inductor
$v_{\mathrm{T,in}}$ - transformer input voltage
$v_{\mathrm{T,out}}$ - transformer output voltage
$Y(s)$ - plant output
z_{GM}, z_{PM} - a complex number corresponding to a certain GM and PM

I. INTRODUCTION

Nowadays power electronics circuits act as controlled interfaces between miscellaneous components or subsystems of electric systems. Their overall control functionality can be split into two sub-functionalities. One is related to the so called state machine responsible for changing of the circuit operation states depending on monitored circuit or its environment conditions. Second sub-functionality is dedicated to the closed loop control of designated quantities and it is a subject to this paper.

The closed loop control mechanism are quite often driven by a regulator which relies on proportional-integral, PI, actions being a part of the proportional-integral-derivative, PID, structure [1]. This type of regulator has proven its usefulness over number of decades - be it in the analogue or the digital domain. Indisputably the regulator is the back bone of the closed loop control and is responsible for the overall loop stability at given circuit configuration. Therefore at this stage there is extensive literature related to its structure selection and gains tuning methods - be it in form of books [1]–[3] or papers [4], [5]. Nevertheless, in this multiplicity of solutions we can lose orientation. Especially when it is necessary to concentrate on an application instead of gains selection methods. Quite often there is a moment of hesitation — which method should I use, does my theoretical background allow me to use it effectively, and so on. No simple answer exists to such questions, although in this work the $\mathfrak{D}$-decomposition technique proposed in 1948 by Neimark [6] and Shafiei and Shenton [7] is considered as a way out. The technique, in opposite to the classical Routh- Hurwitz criterion [8], [9], allows for direct inclusion of time delays into analysis of control loops [10] which are always present in digital control solutions.

To be precise, not only the $\mathfrak{D}$-decomposition on its own is considered but in combination with other commonly used criteria. This is because the $\mathfrak{D}$-decomposition in its original form as a method relying on a frequency sweep test determines asymptotically stable region (or regions) only - this in a space of selected parameters. Here the $\mathfrak{D}$-decomposition mechanism serves as a unification platform offering unambiguous output results format. The format is independent of the input requirements type and it is the controller gains, say

K_P and K_I in case of the PI structure. The considered in this paper input requirements belong to the frequency domain and the time domain. In the frequency domain they are the gain- and the phase-margins, (GM, PM), and the sensitivity, M_S. In terms of the time domain indirect requirements two sets of parameters are considered. They are used for the pole placements description. The first set consists of the real, σ, and the imaginary, ω_d, parts of the Laplace operator, (σ, ω_d). Similarly the second set is constructed with the damping ratio ξ and the undamped natural frequency ω_n, (ξ, ω_n). As the direct time domain requirements the overshoot δ and the rise time t_r are considered, (δ, t_r).

As a sort of challenge related to this approach one may think of symbolic equations processing, if such a form of solution is needed. Nevertheless, for low order plants with a PI compensator, it is easy manageable by mathematical software such as e.g. Wolfram Mathematica or Matlab. In case of higher order plants numerical solutions are more efficient. Another threshold to overcome may be proper interpretation of the graphical results. However, it is well explained in terms of the global stability boundary indication according to [6]. It is important here to follow properly the direction of the frequency change. The above mentioned complementary constraints designate only additional regions within the global stability boundary. The designation relies on the same rules as in case of the global stability.

There are existing works documenting some of the mentioned above combinations although they do not provide consistent overall picture of the pros and cons related to such schemes.

The earliest documentation found by the authors of this paper on the *GM* and *PM* requirements combined with the $\mathfrak{D}$-decomposition mechanism, although not referencing directly to it, is from 1988 [11]. It was done in relation to systems with adjustable parameters. There was no control time delays taken into account and it was without experimental validation. In [12] the authors provide extensive list of references to the D-partition use (name interchangeably used for the $\mathfrak{D}$-decomposition) in the introduction. Later in the paper the σ and the ξ usage is described as criteria for the PI compensator gains selection criteria by means of the $\mathfrak{D}$-decomposition technique. The results demonstrate usefulness of such approach although have not been verified experimentally. Another variant of use of the $\mathfrak{D}$-decomposition was reported in [13]. Here the M_S was used as a parameter guaranteeing control robustness in relation to a fractional-order PI^λ PMSM speed controller. Effectiveness of such approach was confirmed for fixed value of the Θ parameter in simulation. The Θ stands for a vector rotation angle at its value when the circle with radius of $1/M_S$ is tangent to the Nyquist curve. The M_S was also used in [14]. Here the PID regulator for a plant with a delay was tuned and results were confirmed in simulation. Going further, in [15] the H_∞ norm constraint type was used in combination with the $\mathfrak{D}$-decomposition for the three-delay controller gains selection. In this case additional $\Delta\mathfrak{D}_\infty$ singular boundary was used - this as an extension to the $\Delta\mathfrak{D}_0$ discussed later in this paper. Effectiveness of such approach was confirmed in simulation. The $\mathfrak{D}$-decomposition was also used in the z-domain, [16]. Authors demonstrated differences between the stability boundaries of the continuous time solution, without control delays, and the discrete time domain approach with inherited by the definition sampling time delays. The presented analysis demonstrates also interactions between selected control object parameters variations and trajectories basing on boundaries calculated with the time and the frequency domains requirements. The results are verified experimentally with the IPMSM drive current control by means of PI regulators. This publication could be considered as one demonstrating versatility of the $\mathfrak{D}$-decomposition method in the discrete time domain. Nevertheless, the analysis are based on purely numerical and graphical design. There is no unambiguous path leading to the control design tool development. This is somehow justified by complexity of the plant transfer function. What may be disputable in this article is a sentence saying that the D-partition method is correct in the discrete time domain rather than in the continuous time domain. It is truth only if the measurements and the control delays are not taken into account in the open loop transfer function in the continuous time domain.

In this paper the analysis are conducted in the continuous time domain with important delays taken into consideration. As a concept verification object the Dual Active Bridge converter, DAB, output voltage regulator has been selected. The DAB topology, see Fig. 1, is quite common in the electric power conversion solutions where the bidirectional power flow is needed [17]. Its control-to-output transfer function in form of mathematical symbolic equation is not straight forward. The model strongly depends on the control scheme applied [18]. Therefore for purpose of this investigation the transfer function has been selected basing on analysis of experimentally recorded output voltage step response. The identification has been conducted in the circuit under the phase shift control scheme [19].

Given the relative complexity of the analyses, the identified transfer function has been used firstly in two separate scenarios. The 1st scenario was for constraints in the frequency-domain combined with the $\mathfrak{D}$-decomposition mechanism and the 2nd scenario was for the time-domain constraints combined with the $\mathfrak{D}$-decomposition. It allowed to visualise their separated effects in the (K_P, K_I) coordinates. After such an introductory work the final analyses were performed.

This paper is organized as following. The section II contains the DAB converter details with the control-to-output transfer function identified. In the section III the $\mathfrak{D}$-decomposition technique is presented in a systematic way and functions of the K_P and K_I gains are derived step by step to build up sufficient understanding of the approach. Equivalent Nyquist plots are included in this section too just

for better explanation. Then in the section IV mathematical modelling and experimental results with the PI and the IP regulators are presented and discussed. Finally conclusions are given in section V.

II. THE DUAL ACTIVE BRIDGE CONVERTER AS A CONTROL OBJECT

A. GENERAL CIRCUIT INFORMATION

The output voltage of the Dual Active Bridge converter, $v_{\mathrm{DAB,out}}$, shown in Fig. 1 has been chosen to be controlled by means of a PI compensator.

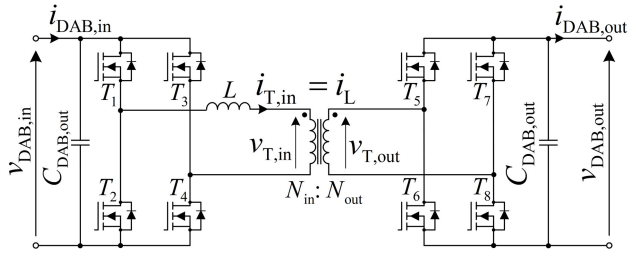

FIGURE 1. General block diagram of the dual active bridge converter.

The DAB converter consists of: (i) two H-bridge inverters with DC-sides capacitive filters, (ii) a medium frequency transformer with turns ratio $N_{\mathrm{T,in}}/N_{\mathrm{T,out}}$, (iii) inductance L, (iv) overall control section responsible for the feedback signals measurement and processing followed by the regulation, (v) modulation and transistor gate drive section. The L in this case is to be understood as a sum of an auxiliary inductance and the transformer leakage inductance referred to the input side. Such circuit is capable of bidirectional power flow by means of proper control. In this paper, for simplicity reasons, power is assumed to be transferred from the input to the output side only.

The converter operates under control method called Phase Shift Modulation, PSM, [20]. The PSM is based on variation of the phase shift $\varphi_{\mathrm{DAB,out}}$ between the input and output gate drive sections. This influences the voltage v_{L} and in consequence the current i_{L} across the inductance, see Fig. 2. By such the power transfer is controlled too. The subscript $\cdot_{\mathrm{DAB,out}}$ indicates that the output side signals are shifted in reference to their input equivalents, $\varphi_{\mathrm{DAB,in}} = 0$, see Fig. 3. The phase shift is set by a PI regulator. All the duty cycles of the gate drive signals, $D_{\mathrm{DAB,in}}$ and $D_{\mathrm{DAB,out}}$, are set to 50%. A dead time $T_{\mathrm{dt}} = 1\mu\mathrm{s}$ has been applied between the upper and the lower gate drive signals in order to avoid the short circuits in between switching. Such a basic control scheme may call for extension in order to compensate the dc-bias inductor current, especially when low on-state resistance MOSFET switches are used [21].

The test circuit used in this research relied on DAB architecture with IGBT switches driven by the PWM signals at frequency $f_{\mathrm{s}} = 16\ kHz$. The rated input and output voltages were $V^{\mathrm{rtd}}_{\mathrm{DAB,in}} = 100\ V$ and $V^{\mathrm{rtd}}_{\mathrm{DAB,out}} = 50\ V$. More details about the circuit parameters can be found in Table 3.

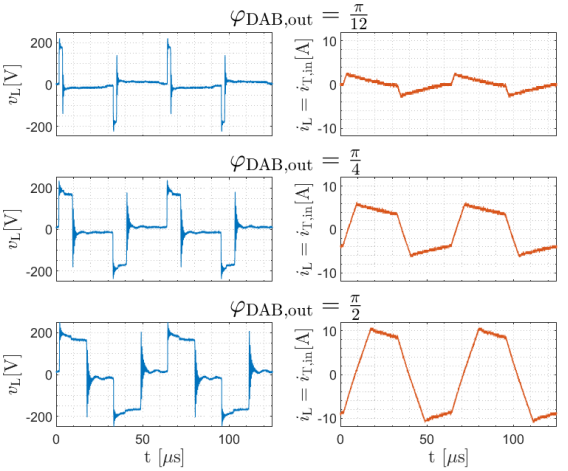

FIGURE 2. Visualization of voltage and current across the inductance L under the Phase Shift Modulation, PSM, control. The records are from investigated experimental setup at three different phase shifts, $\varphi_{\mathbf{DAB,out}} \in \{\pi/12, \pi/4, \pi/2\}$.

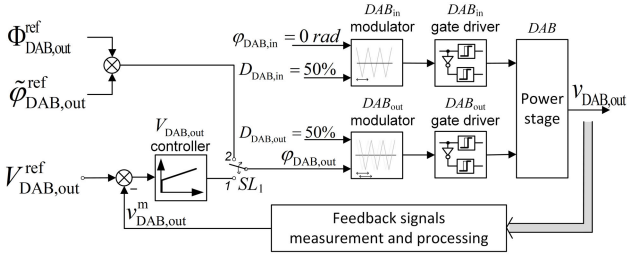

FIGURE 3. Simplified block diagram of the test setup configurations: scenario No. I) - selector SL_1 in position 2 for the control-to-output experimental transfer function identification, $P^{\mathrm{exp,est,c2o}}_{\mathbf{DAB}}(s)$; scenario No. II) selector SL_1 in position 1 for tests of the closed loop output voltage control.

B. IDENTIFICATION OF THE CONTROL-TO-OUTPUT TRANSFER FUNCTION

Detailed mathematical modelling of the DAB was not an objective of this research therefore its control-to-output transfer function, $P^{\mathrm{exp,est,c2o}}_{\mathrm{DAB}}(s)$, has been estimated from experimentally measured step response of the output voltage. The experiment was conducted according to scenario No. I from Fig. 3. Measured voltage, shown in Fig. 4 as $v^{\mathrm{exp,m,c2o}}_{\mathrm{DAB,out}}$, was recorded at output power point equal to $370W$ with $\varphi_{\mathrm{DAB,out}}$ step change from $0.698rad$ to $0.820rad$. Such a range was equivalent to the output voltage change from $45V$ to $50V$.

Basing on the response measured a transfer function (1) has been obtained. The $P^{\mathrm{exp,est,c2o}}_{\mathrm{DAB}}(s)$ has been quantified with Matlab/Simulink 'ident' toolbox, using 'tfest' function. For purpose of the quantification, the first order model was assumed - this basing on visual inspection of the physical response character.

$$P^{\mathrm{exp,est,c2o}}_{\mathrm{DAB}}(s) = \frac{40.93}{s0.021 + 1} \tag{1}$$

The (1) can easily be converted to the $\frac{1949.05}{s+47.62}$ format although for simplicity reasons is not used as such in this

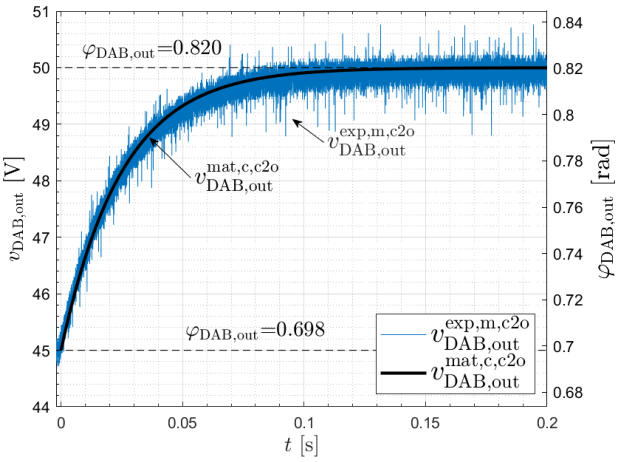

FIGURE 4. Voltage step responses of the estimated control-to-output DAB transfer function, $P^{exp,est,c2o}_{DAB}(s)$ as per (1) and the experimentally measured $v^{exp,m,c2o}_{DAB}$ in a prototype circuit with parameters as per Table 3. The voltages are recorded for $\Phi^{ref}_{DAB,out}$ step command change equivalent to the output voltage change from 45*V* to 50*V*. The test was performed with control circuit configuration according to scenario No. I shown in Fig. 3.

paper. In this work, we want to operate on the plant's time constant directly. The equivalent format will be used in our future works leading to formulation of more generalised gains selection rules.

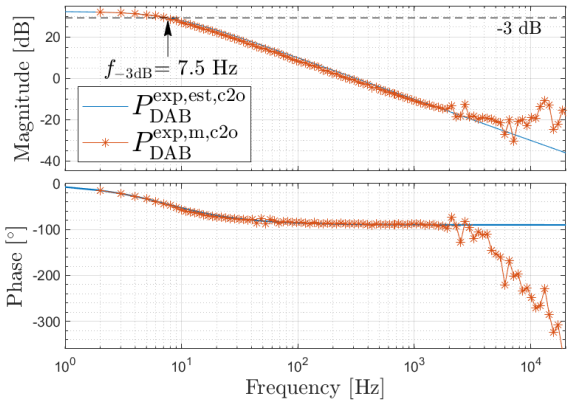

FIGURE 5. The bode plot of the identified DAB control-to-output transfer function (1), $P^{exp,est,c2o}_{DAB}(s)$, for the operating power point equal to the converter rated power P^{rtd}_{DAB} = 400 W.

The Bode plots of (1) at the converter rated power, P^{rtd}_{DAB}, can be seen in Fig. 5. The $-3dB$ point is located at frequency of $7.5Hz$ and its corresponding phase shift is equal to $45°$. The measured values at higher frequencies are strongly affected by the measurement equipment bandwidth. Nevertheless the medium frequency range is in good correlation with the identified transfer function results. This together with comparison shown in Fig. 4 was considered as a sufficient confirmation of (1).

III. DESIGN OF OUTPUT VOLTAGE PI CONTROLLER WITH $\mathfrak{D}$-DECOMPOSITION TECHNIQUE

A. GENERAL INTRODUCTION TO THE NEIMARK's $\mathfrak{D}$-DECOMPOSITION TECHNIQUE IN PRESENCE OF THE CIRCUIT TIME DELAYS

Neimark's $\mathfrak{D}$-decomposition technique (or D-partition technique) establishes direct correlation between the characteristic equation and the space of permissible parameters for which the stability is guaranteed [22]. In other words by means of this technique one can reach such characteristic equation roots locations on the s-plane that they guarantee presence at the stability boundary.

In order to calculate boundary of the stable region it is necessary to substitute $s = j\omega$ in the characteristic equation, where $\omega = 2\pi f$ is a real number in range $-\infty < \omega < +\infty$. Such equation, or rather its real and imaginary parts, must be equated to zero. Solution of these equations leads to dependencies describing a parametric hypersurface which precisely designates a boundary in a so called $\mathfrak{D}$ surface. The parametric surface defined as $D(l, r = n - l)$, with l and r standing for number of n^{th}-order characteristic equation roots in the left and right half-plane respectively, becomes $D(l = n, 0)$ if $r = 0$. Such defined surface unambiguously indicates stable region [22].

Having the stability boundary it is necessary to find out now on which side the stable area is. This can be done using the original Neimark's guidelines [6]. For a single parameter it says that: when drawing the boundary of the parametric hypersurface (by changing frequency in direction from $-\infty$ to $+\infty$) then the left-hand side of the boundary is the stable region. It indicates the whole asymptotic stability region. For two changing parameters (say proportional and integral gains of a PI compensator), $m = 2$, an additional boundary is needed. This can be achieved by introducing a $\Delta\mathfrak{D}_0$ $(m-2)$-dimensional hyperplane [6]. The $\Delta\mathfrak{D}_0$ hyperplane is related to the characteristic equation having a real zero at the origin of the s-plane ($s = 0$). Solving such relation leads to indication of complementary criterion for the second parameter region.

In case if particular GM and PM are to be applied an additional dedicated boundary must be derived in order to narrow the asymptotic stability region. It can be realized with guidelines given in [23]. To do so, it is necessary to equate the characteristic equation to a complex number representing desired GM and PM, this instead of equating it to zero. In such case the formulated equation is called "relative characteristic equation", RCE, [23].

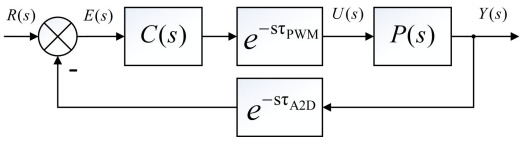

FIGURE 6. Block diagram of closed loop control structure with the PWM and A2D delays.

For figurative explanation an example with classical control structure with time delays as shown in Fig. 6 will be

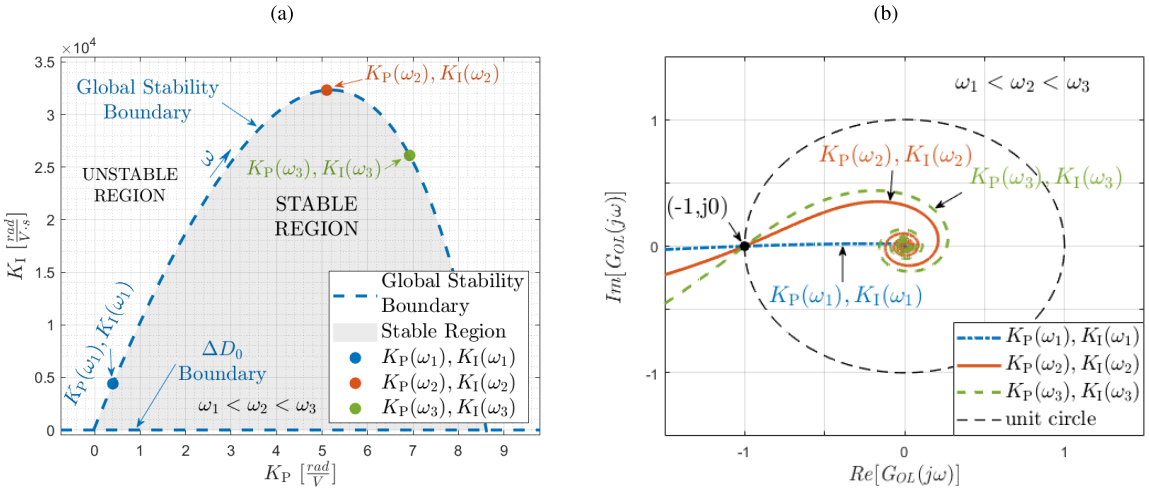

FIGURE 7. Visualisation of the global stability boundary (a) calculated using the $\mathfrak{D}$-decomposition technique together with corresponding to it Nyquist plots (b). They are based on a system with time delays shown in Fig. 6. For better understanding of relations between the $\mathfrak{D}$-decomposition and the Nyquist plots three different sets of gains ($K_P(\omega)$, $K_I(\omega)$) have been drawn. They are related to three different pulsations, $\omega \in (\omega_1, \omega_2, \omega_3)$.

used. The closed-loop transfer function of the above control structure can be written in the Laplace domain as:

$$G_{\mathrm{CL}}(s) = \frac{C(s)e^{-s\tau_{\mathrm{PWM}}}P(s)}{1 + C(s)e^{-s(\tau_{\mathrm{PWM}}+\tau_{\mathrm{A2D}})}P(s)} \tag{2}$$

where: $C(s)$ is the regulator transfer function; $P(s)$ is the controlled plant transfer function; $R(s)$ is reference signal; $E(s)$ is the error; $U(s)$ is control signal; $Y(s)$ is the plant output, τ_{A2D} is the Analogue-to-Digital conversion delay, τ_{PWM} is the time delay related to discontinuous nature of the Pulse Width Modulation, PWM. As a common practice, the time constant τ_{PWM} is assumed to be somewhere between 0.5 to 1 times one over the switching frequency. In our case $\tau_{\mathrm{PWM}} = 1 \cdot 1/16kHz = 62.5\mu s$. The $\tau_{\mathrm{A2D}} = 1 \cdot 1/32kHz = 31.25\mu s$ as all the measurement and control calculation tasks are executed within a half time of the switching period.

Now, we assume that the plant transfer function corresponding to (1) is:

$$P(s) = \frac{Y(s)}{U(s)} = \frac{K}{sT_{\mathrm{o}} + 1} \tag{3}$$

where: K and T_{o} are an identified transfer function parameters - the steady state plant gain and the plant time constant respectively. The proportional-integral, PI, compensator transfer function can be written as:

$$C(s) = K_{\mathrm{P}} + \frac{K_{\mathrm{I}}}{s} \tag{4}$$

where K_{P} is the proportional gain and K_{I} is the integral gain. In such case the equation (2) can be rewritten as:

$$G_{\mathrm{CL}}(s) = \frac{K(sK_{\mathrm{P}} + K_{\mathrm{I}})e^{-s\tau_{\mathrm{PWM}}}}{s^2T_{\mathrm{o}} + s(KK_{\mathrm{P}}e^{-s\tau} + 1) + KK_{\mathrm{I}}e^{-s\tau}} \tag{5}$$

where the denominator is the characteristic equation with the -1 comprised inside and the $\tau = \tau_{PWM} + \tau_{A2D}$.

The characteristic equation in general form, with $s = j\omega$ in the frequency domain, can be written as by means of the open loop transfer function, G_{OL}, with three arguments:

$$G_{\mathrm{OL}}(j\omega, K_{\mathrm{P}}, K_{\mathrm{I}}) + 1 = 0 \tag{6}$$

The above equation can be rewritten in the form used in the Nyquist plot analysis as:

$$G_{\mathrm{OL}}(j\omega, K_{\mathrm{P}}, K_{\mathrm{I}}) = -1 + j0 \tag{7}$$

where the $-1 + j0$ instead of -1 is written only to emphasize that the imaginary part exists but is equal to zero. Remembering that, the equation (7) can be written as following two equations:

$$\Re\mathfrak{e} = [G_{\mathrm{OL}}(j\omega, K_{\mathrm{P}}, K_{\mathrm{I}})] = -1 \tag{8}$$

$$\Im\mathfrak{m} = [G_{\mathrm{OL}}(j\omega, K_{\mathrm{P}}, K_{\mathrm{I}})] = 0 \tag{9}$$

Solving the (8) and (9) for the K_{P} and K_{I} leads to equations describing the parametric hypersurface designating the stability boundary on the $\mathfrak{D}$ surface:

$$K_{\mathrm{P}}(\omega) = \frac{-\cos\left((\tau_{\mathrm{PWM}} + \tau_{\mathrm{A2D}})\,\omega\right)}{K} + \frac{\omega\, T_{\mathrm{o}} \sin\left((\tau_{\mathrm{PWM}} + \tau_{\mathrm{A2D}})\,\omega\right)}{K} \tag{10}$$

$$K_{\mathrm{I}}(\omega) = \omega\left[\frac{\omega\, T_{\mathrm{o}} \cos\left((\tau_{\mathrm{PWM}} + \tau_{\mathrm{A2D}})\,\omega\right)}{K} + \frac{\sin\left((\tau_{\mathrm{PWM}} + \tau_{\mathrm{A2D}})\,\omega\right)}{K}\right] \tag{11}$$

Obtained functions for the K_{P} and K_{I} are dependent on the circuit delays. Plot of (10) and (11) with frequency as a parameter changing from $-\infty$ through 0 to $+\infty$ can be seen in Fig. 7(a). The stable region is on the left-hand side of the boundary - this when moving with ω from $+\infty$ to 0.

For the two parameters considered such boundary must be complemented by one more limit. The additional limit is

driven by the $\Delta\mathfrak{D}_0$ hyperplane. As mentioned before, it can be designated by comparison of the characteristic equation to 0 at the origin of the s-plane ($s = 0$). Basing on (5) it can be written:

$$\Delta\mathfrak{D}_0 \Rightarrow KK_\mathrm{I} = 0 \tag{12}$$

The equations (10)..(12) are completely describing the parametric hypersurface designating the stability boundary on the $\mathfrak{D}$ surface.

The three example points in Fig. 7(a), at frequencies $\omega_{1..3}$, are located exactly on the stability boundary. This is confirmed by corresponding Nyquist characteristics shown in Fig. 7(b). The three plots cross the $(-1, j0)$ point what indicates that the circuit is at the stability boundary. One should notice that the spiral characteristics of different $(K_\mathrm{P}, K_\mathrm{I})$ pairs surround the point $(0, j0)$ which in this case is driven by the delays.

B. THE $\mathfrak{D}$-DECOMPOSITION TECHNIQUE WITH THE GAIN AND PHASE MARGINS AS THE FREQUENCY DOMAIN CONSTRAINTS

Basic stability criteria in the frequency domain are the gain margin, GM, and the phase margin, PM, [2]. They are intuitive and very often applied during control design to ensure certain safety margins of the open-loop system which will become a closed-loop one [24]–[26]. This makes them worthy candidates for merge with the $\mathfrak{D}$-decomposition technique. It can be done by replacing the point $(-1, j0)$ in equation (7) with a certain location on the complex surface.

$$G_\mathrm{OL}(j\omega, K_\mathrm{P}, K_\mathrm{I}) = a + jb \tag{13}$$

where $a + jb$ stands for desired location of an arbitrary point in the Cartesian coordinates. For certain GM, expressed in decibels, dB, it can be written:

$$\begin{aligned} a_\mathrm{GM} &= -10^{\frac{-GM}{20}} \\ b_\mathrm{GM} &= 0 \end{aligned} \tag{14}$$

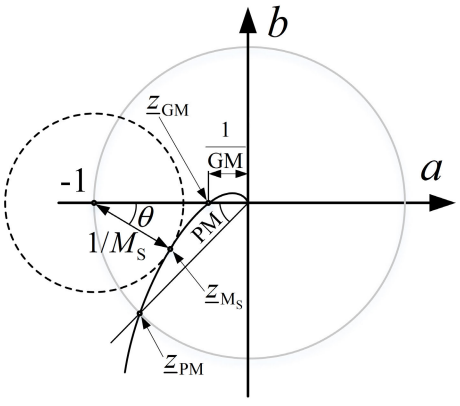

FIGURE 8. Visualization of the gain and phase margins, *GM PM*, and the sensitivity, M_S concepts by means of the nyquist plot.

The expression (14) can be represented in a graphical form, in polar coordinates, as shown in Fig. 8. Such location can be easily translated into the Nyquist plot as a complex number $\underline{z}_\mathrm{GM} = a_\mathrm{GM} + jb_\mathrm{GM}$. Similarly, the PM in degrees, °, can be calculated according to:

$$\begin{aligned} a_\mathrm{PM} &= \cos\left(\frac{2\pi PM}{360} + \pi\right) \\ b_\mathrm{PM} &= \sin\left(\frac{2\pi PM}{360} + \pi\right) \end{aligned} \tag{15}$$

The expression (15) is equivalent to graphical representation in polar coordinates as shown in Fig. 8. It can also be translated into the Nyquist plot by means of substitution $\underline{z}_\mathrm{PM} = a_\mathrm{PM} + jb_\mathrm{PM}$.

By substituting (14) into (13), the K_P and K_I gains of the first order plant, with the time delays and GM, can be calculated:

$$K_\mathrm{P}(\omega, \mathrm{GM}) = 10^{-\left(\frac{GM}{20}\right)}\left[\frac{-\cos\left((\tau_\mathrm{PWM} + \tau_\mathrm{A2D})\,\omega\right)}{K} + \frac{\omega\, T_\mathrm{o} \sin\left((\tau_\mathrm{PWM} + \tau_\mathrm{A2D})\,\omega\right)}{K}\right] \tag{16}$$

$$K_\mathrm{I}(\omega, \mathrm{GM}) = 10^{-\left(\frac{GM}{20}\right)}\omega\left[\frac{\sin\left((\tau_\mathrm{PWM} + \tau_\mathrm{A2D})\,\omega\right)}{K} + \frac{\omega\, T_\mathrm{o} \cos\left((\tau_\mathrm{PWM} + \tau_\mathrm{A2D})\,\omega\right)}{K}\right] \tag{17}$$

Similarly, by substituting (15) into (13), equations for K_P and K_I with PM taken into account can be derived:

$$K_\mathrm{P}(\omega, PM) = \frac{-\cos(\frac{2\pi PM}{360} + (\tau_\mathrm{PWM} + \tau_\mathrm{A2D})\omega)}{K} + \frac{\omega T_\mathrm{o} \sin(\frac{2\pi PM}{360} + (\tau_\mathrm{PWM} + \tau_\mathrm{A2D})\omega)}{K} \tag{18}$$

$$K_\mathrm{I}(\omega, PM) = \omega\left[\frac{\omega T_\mathrm{o} \cos(\frac{2\pi PM}{360} + (\tau_\mathrm{PWM} + \tau_\mathrm{A2D})\omega)}{K} + \frac{\sin(\frac{2\pi PM}{360} + (\tau_\mathrm{PWM} + \tau_\mathrm{A2D})\omega)}{K}\right] \tag{19}$$

Graphical representation of equations (16) and (17) for a fixed GM and variable pulsation ω can be seen in Fig. 9(a). Corresponding Nyquist plots are shown in Fig. 9(b). The same can be seen for equations (18) and (19) in Fig. 9(c) and (d). Obviously if certain GM and PM requirements are to be fulfilled together then we must look for a cross point of the two plots - if such a solution exists. The limit driven by the $\Delta\mathfrak{D}_0$ hyperplane is not affected by the GM and PM requirements.

Equations (16)..(19) describing K_P and K_I as functions of ω and GM or PM may be considered as an extension of the original $\mathfrak{D}$-decomposition technique [27]. Of course they can be used for the global stability boundary calculation when the GM and PM are equal to zero. Presence of GM and PM values greater than zero cause changes of the suitable gains region as shown in Fig. 10 (b) and (d). The region shrinks as the margins rise, while the $\Delta\mathfrak{D}_0$ limit is not affected - this as expected. That of course finds its reflection in the polar plain

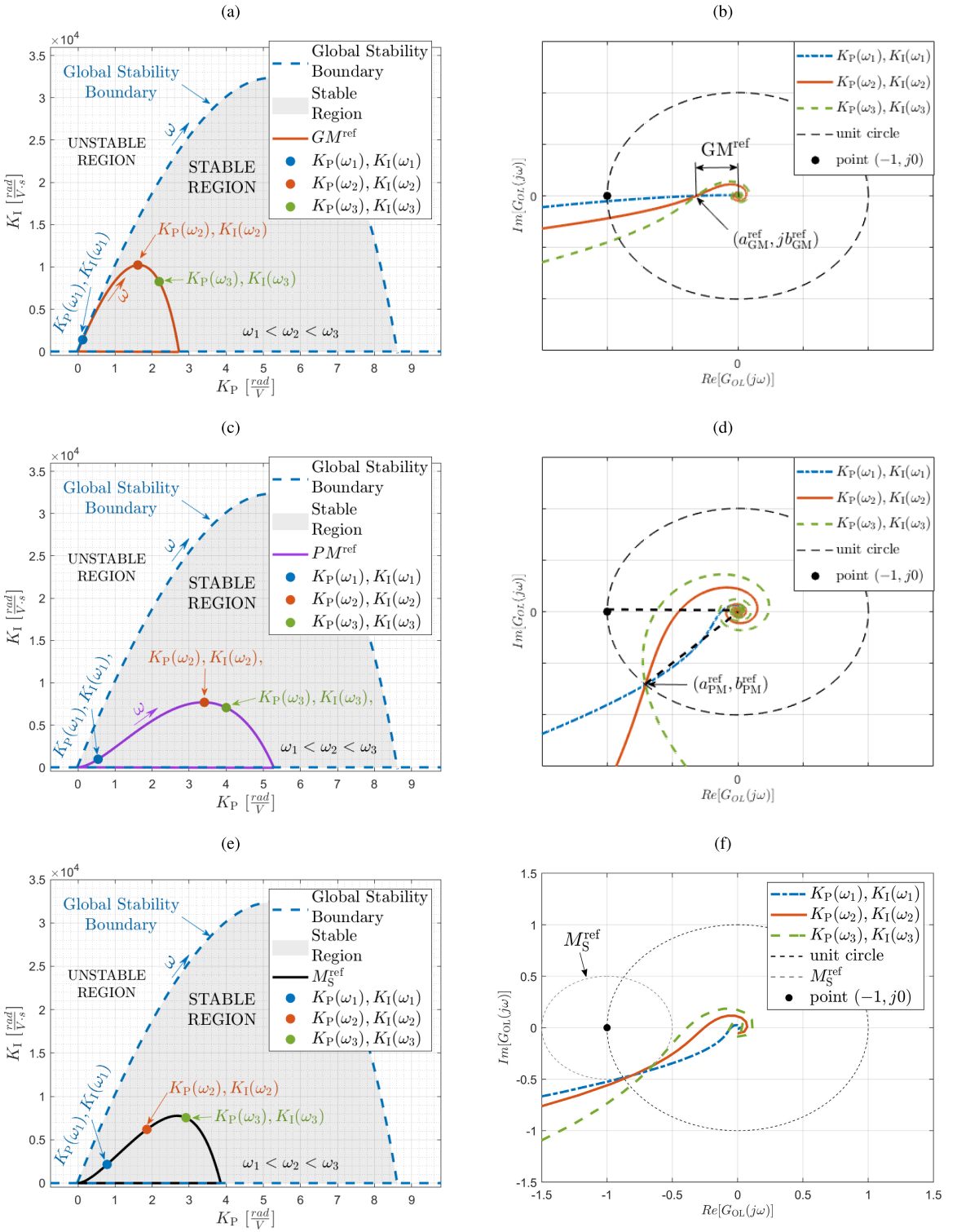

FIGURE 9. Visualisation of the gain margin, *GM*, the phase margin, *PM*, and the sensitivity M_S trajectories against the global stability boundaries (a, c, e) - calculated using the $\mathfrak{D}$-decomposition technique. Corresponding Nyquist plots are (b)→(a), (d)→(c) and (f)→(e). The plots belong to a control structure with delays shown Fig. 6. For better understanding of relations between the $\mathfrak{D}$-decomposition and the Nyquist plots three different sets of gains ($K_P(\omega)$,$K_I(\omega)$) have been drawn on the *GM*, *PM* and the M_S trajectories. They are related to three different pulsations, $\omega = \{\omega_1, \omega_2, \omega_3\}$.

representation as shown in Fig. 10 (a), $GM = \langle 0dB,\ +\infty)$, and Fig. 10 (c), $PM = \langle 0°,\ 90°)$.

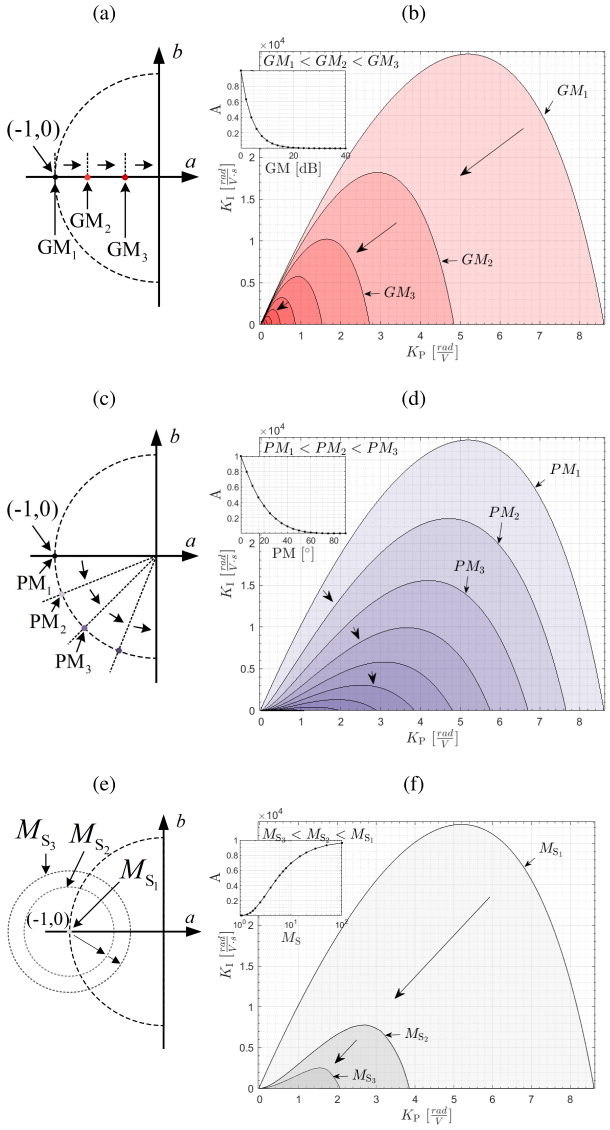

FIGURE 10. Visualization of Neimark's $\mathfrak{D}$-decomposition technique mechanism applied to calculate (i.) stability boundaries and (ii.) trajectories of desired frequency domain driven control margines, (b) for *GM*, (d) for *PM*, (f) for M_S, for 1st−order plant with a PI compensator and delays according to Fig. 6. The (a), (c) and (e) are simplified Nyquist plot equivalents. Additional plots of areas *A* are shown for better understanding of the changes nature.

C. THE $\mathfrak{D}$-DECOMPOSITION WITH THE SENSITIVITY AS A CONSTRAINT IN THE FREQUENCY DOMAIN

Another common approach, or even complementary one, to design of a closed loop control relies on a parameter called sensitivity margin, M_S [28]. The M_S as a criterion accounted to the frequency domain makes sure that there is a certain robustness against the plant dynamics variation driven by its parameters change. In terms of definitions used in the control literature it can be accounted to the Θ-stability [29]. In a graphical way, as a general explanation, it can be shown as in Fig. 8. In terms of mathematical expression it can be written as a complex number $\underline{z}_{M_S} = a_{M_S} + jb_{M_S}$. Therefore a point in Nyquist plot can be calculated according to the real and imaginary parts represented as following [30]:

$$\begin{aligned} a_{M_S} &= -1 + \frac{1}{M_S}\cos(-\theta) \\ b_{M_S} &= \frac{1}{M_S}\sin(-\theta) \end{aligned} \tag{20}$$

where the θ can be understood as an angular position of the rotating $\frac{1}{M_S}$ vector. Now, by substituting the (20) into (7) we obtain another functions for the K_P and K_I:

$$K_P(\omega, M_S, \theta) = \frac{-\sin(-\theta)A_1 + \cos(-\theta)(-A_2)}{KM_S} + \frac{A_2}{K} \tag{21}$$

$$K_I(\omega, M_S, \theta) = \frac{\omega A_1}{K} + \frac{\omega(-\cos(-\theta)A_1) + \omega(\sin(-\theta)A_2)}{KM_S} \tag{22}$$

where:

$$\begin{aligned} A_1 &= \omega T\cos(\omega(\tau_{PWM} + \tau_{A2D})) + \sin(\omega(\tau_{PWM} + \tau_{A2D})) \\ A_2 &= T\omega\sin(\omega(\tau_{PWM} + \tau_{A2D})) - \cos(\omega(\tau_{PWM} + \tau_{A2D})) \end{aligned}$$

Obtained functions lead to results shown in Fig. 9 (e) and (f). Aforementioned drawings for different values of the M_S while changing the pulsation ω can be also seen in Fig. 10 (e) and (f). For the sake of better qualitative explanation three different M_S levels have been shown. The M_{S_1} stands for the zero value. It results in the same trajectory as the stability boundary. Increase of its value leads to decrease of the stable area. This is as intuitively expected while looking at results for the *GM* and *PM* shown in in the same figure. The area *A* has been also shown here for better visualisation.

D. THE $\mathfrak{D}$-DECOMPOSITION WITH THE POLE PLACEMENTS AS THE TIME DOMAIN CONSTRAINS

Another practical way of characterising the dynamic response of a system under control is analysis of the pole placements in the s-plane. The $\mathfrak{D}$-decomposition technique can indirectly utilize requirements driven by such. Obtained overall results are equivalent to the Γ-stability, [29], outcomes although they are in the intuitive (K_P, K_I) parametric plane.

The pole placements can be described in two ways. One of them relies on substituting following expression for s (instead of $s = j\omega$) in (7):

$$s = -\sigma \pm j\omega_d \tag{23}$$

where: σ and ω_d is the real and the imaginary part of Laplace operator respectively. The ω_d is the damped natural frequency. Such approach is reported in literature as the σ-stability [12], [31]. It has its direct foundation in the Hurwitz-stability concept [29] and therefore it could be classified as a sub-criterion of the Γ-stability.

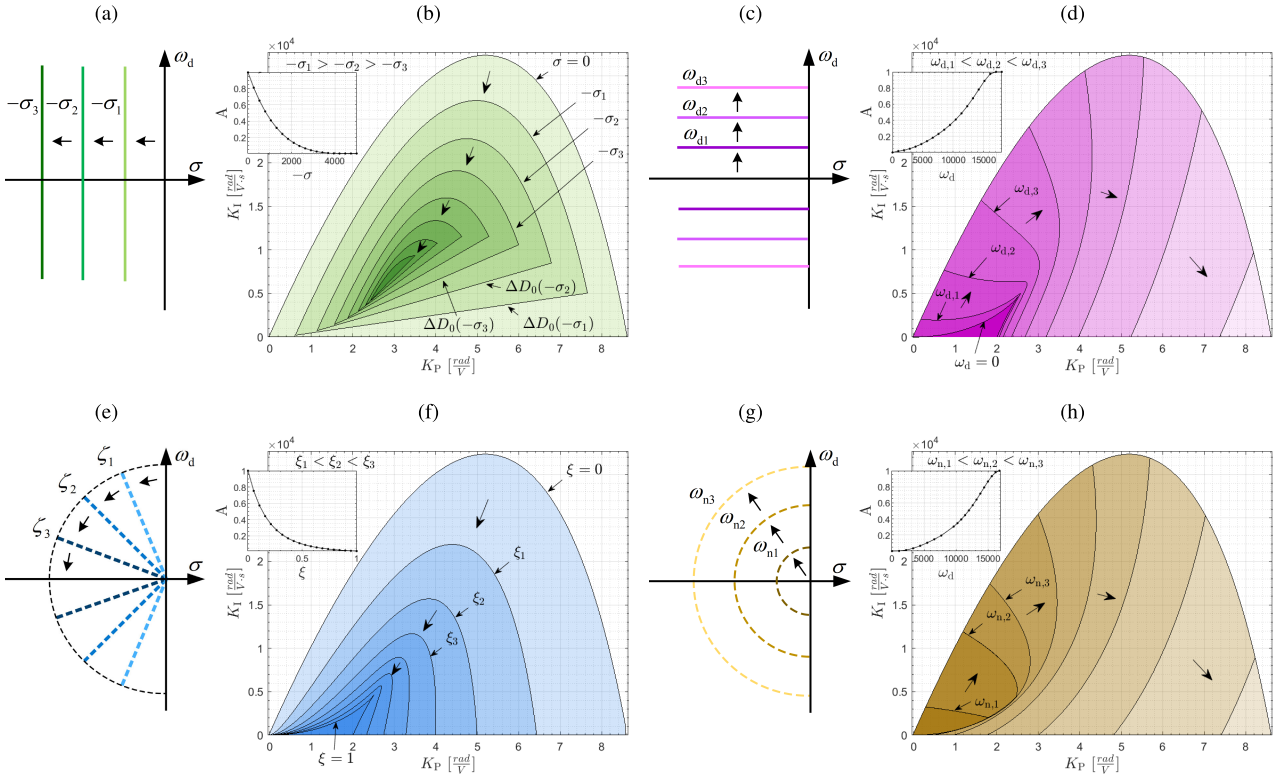

FIGURE 11. Visualization of Neimark's $\mathfrak{D}$-decomposition technique method applied to calculate (i.) stability boundaries and (ii.) trajectories of the s-domain driven control margines for 1^{st}–order plant with a PI compensator and delays according to Fig. 6. The (a), (c), (e) and (g) are the *s*-plane equivalents. The *s* is to be understood as the left half-plane described by (23) for (a) to (c) and by (27) for (e) to (g). The (b) and (d) plots show parametrised trajectories corresponding to substitution $s = -\sigma \pm j\omega_d$, with σ and ω_d parameters respectively. The (f) and (h) plots show parametrised trajectories corresponding to substitution $s = -\xi\omega_n \pm j\omega_n\sqrt{1-\xi^2}$, with ξ and ω_n parameters respectively. Surface areas *A* are shown for better visualization.

Solving the (7), taking into account (23), leads to K_P and K_I functions:

$$K_P(\sigma, \omega_d) = -e^{\sigma\tau}\left(\frac{\omega_d(1+2\sigma T)\cos[\omega_d\tau]}{\omega_d K} + \frac{(\sigma+\sigma^2 T-\omega_d{}^2 T)\sin[\omega_d\tau]}{\omega_d K}\right) \quad (24)$$

$$K_I(\sigma, \omega_d) = e^{\sigma\tau}\frac{(\sigma^2+\omega_d^2)}{\omega_d K}\cdot[\omega_d T\cos(\omega_d T) + (1+\sigma T)\sin(\omega_d T)] \quad (25)$$

As before, the equations (24) and (25) indicate regions with constraints in the s-domain but this time by means of σ and ω_d which precisely define complex poles. Basing on the two equations plots shown in Fig. 11(b) and (d) can be drawn. The Fig. 11(b) is for case when the σ is a constant parameter as shown in Fig. 11(a), while ω_d varies in range $\langle 0, +\infty)$, with direction indicated. In this case the calculated trajectories of constant σ parameter are also shaped by the $\Delta\mathfrak{D}_0$ which is dependent on the σ parameter too:

$$\Delta\mathfrak{D}_0 \Rightarrow K_P(\sigma) = \frac{K_I}{\sigma} + \frac{e^{-\sigma(\tau_{PWM}+\tau_{A2D})}(-1+T_o\sigma)}{K} \quad (26)$$

One should notice that the (26) is not a function of the ω_d and affects the K_P function only.

On the other hand, when the ω_d is a constant parameter, as depicted in Fig. 11(c), and σ is changing in range of $\langle 0, +\infty)$ the trajectories look like in Fig. 11(d). In this case the global stability boundary is calculated when $\sigma = 0$ and ω_d varies in range $\langle 0, +\infty)$. Combination of trajectories shown in Fig. 11(b) and (d) leads to selection of the gains ensuring desired dynamic properties.

In terms of the second-order differential equations the above considerations can be translated to even more intuitive terms, namely the damping ratio, ξ, and undamped natural frequency, ω_n. This can be considered as a second way of describing the pole placement. It can be achieved by rearranging the (23) as following:

$$s = -\xi\omega_n \pm j\omega_n\sqrt{1-\xi^2} \quad (27)$$

where: $\sigma = \xi\omega_n$ and $\omega_d = \omega_n\sqrt{1-\xi^2}$. Using equation (27) in $\mathfrak{D}$-decomposition technique leads to results shown in Fig. 11 (f) and (h). Formulas derived for the K_P and K_I are too complex to be shown in the article. Nevertheless desired locations of ξ, Fig. 11 (e), and ω_n, Fig. 11 (g), can be easily applied in a numeric manner with the parameters preprocessing according to the relations between the

(27) and (23). The ω_n and ξ will also be used as a direct link to the time domain constrains represented by the rise time t_r and the overshoot δ. They may be roughly approximated to ω_n and ξ [32], [33]:

$$\omega_n = \frac{1.8}{t_r} \tag{28}$$

$$\xi = -\frac{\log\left(\frac{\delta}{100}\right)}{\sqrt{\log^2\left(\frac{\delta}{100}\right) + \pi^2}} \tag{29}$$

Once again, one should remember that the formulas (27), (28) and (29) are for the second-order differential equations.

IV. EXPERIMENTAL VALIDATION OF THE GAINS SELECTION PROCEDURES BASING ON A DAB CONVERTER CONTROL

Derived formulas based on the $\mathfrak{D}$-decomposition technique with constraints in the frequency and the time domains were verified during selection of the DAB converter controller gains. The gains were calculated taking into account time delays as shown in Fig. 6. It is worth to emphasize, that the transfer function (5) represents a second-order differential equation with a zero. In such case the PI compensator is often implemented as the IP structure [34], [35] shown in Fig. 15. Therefore two validation scenarios have been investigated.

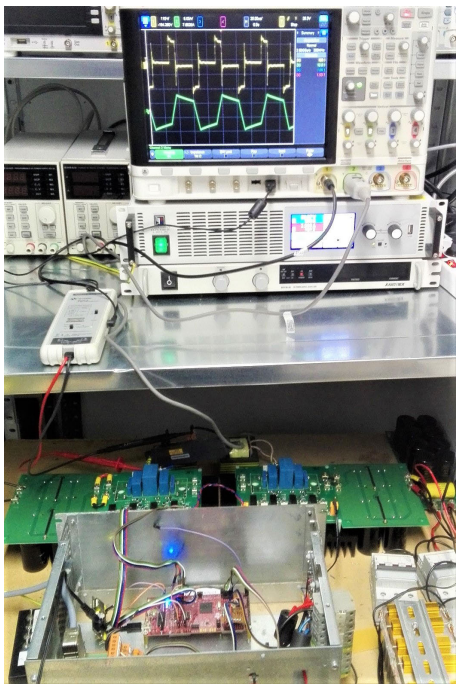

FIGURE 12. Laboratory setup.

The verifications took place in a mathematical model and in an experimental laboratory setup shown in Fig. 12. The mathematical model, with τ_{A2D} and τ_{PWM} delays, relied on the identified transfer function (1) and compensators without limited outputs. The main purpose of such a mathematical model was to show some undisturbed picture of control situation in relation to the $\mathfrak{D}$-decomposition technique combined with tuning criterions considered. The experimental tests were performed at the rated output power of the DAB converter, $P^{rtd}_{DAB,out} = 370W$, with $\pm 10\%$ voltage steps around the rated output voltage, $V^{rtd}_{DAB,out} = 50\ V$, and this after initial voltage step command from $30V$ to $50V$. Along with evaluation of considered gains selection procedures the mathematical model was validated too. This took place basing on its comparison with corresponding experimental results. In both cases the maximum sensitivity M_S level was assumed to not exceed value of 1.4, $M_S \leq 1.4$. The limit is within a typical range recommended in [30].

A. STANDARD PI COMPENSATOR CONFIGURATION

Initially the standard PI compensator gains have been selected using the *GM* and *PM* criteria according to (16)..(19). Desired margins ranges were set to $GM = \langle 45, 50\rangle$dB and $PM = \langle 60, 80\rangle^\circ$. Four sets of K_P and K_I gains indicated by intersection points of the desired trajectories can be seen in Fig. 13 (a). The points are called further on in this article as A, B, C and D. They are all below the maximum sensitivity curve which is indicated as grey area in the plot. Their M_S is slightly above one. The gains and other parameters values are given in the Tab. 1. The table contains also demanded (dem-superscript), calculated (c-superscript) and measured (m-superscript) values of overshoot, δ, and rise time, t_r, coming from mathematical model (mat-superscript) and experiment (exp-superscript). The auxiliary values are obtained from the indicated in the table equations and from output voltage step responses shown in Fig. 14 (a).

Similarly the t_r^{dem} and δ^{dem} parameters related to the ω_n and ξ respectively were used as the time-domain criteria for the PI compensator gains selection. They were specified as following ranges: $t_r^{dem} = \langle 18, 23\rangle$ms and $\delta^{dem} = \langle 0, 4.6\rangle\%$. The ranges are equivalent to $\omega_n = \langle 100, 78.26\rangle$rad/s and $\xi = \langle 0.7, 1\rangle$ respectively accordingly to (28) and (29). The values indicated another four sets of gains called here E, F, G and H points. They are shown in Fig. 13 (b). All of them are also below the maximum sensitivity curve and their M_S are slightly above one too. Values of the gains are listed in the Tab. 1 - this together with the other calculated and measured values. The measured values are from the output voltage step responses shown in Fig. 14 (b).

All plots from Fig. 14 indicate stable control loop operation. They also show practically sufficient correlation between mathematical model and experimental results, although there are points where the results are somehow different.

Comparing the rise times in Tab. 1 one can see that mathematical model responses are generally faster. This is as expected because there is no compensator output limits and the identified transfer function does not take into account all the subtle real world circuit effects. Especially those influencing the high frequency dynamics. The biggest

TABLE 1. Selected K_P and K_I gains of a PI output voltage regulator of a DAB converter - this with use of Neimark's $\mathfrak{D}$-decomposition technique. Points A-D are related to the frequency domain constrains, *GM* and *PM*, see (Fig. 13a) while points E-H come from the time domain constrains such as the rise time t_r and overshoot δ, see Fig. 13 (b). The input requirements are in **bold**. The table also contains associated experimentally measured and calculated parameters with annotations. Points with 'sat' subindex denote the controller output saturation during experimental tests.

Parameter	Unit	$A_{(SAT)}$	$B_{(SAT)}$	C	D	E	$F_{(SAT)}$	G	H
K_P	$[\frac{rad}{V}]$	0.072	0.072	0.041	0.041	0.047	0.078	0.033	0.057
K_I	$[\frac{rad}{Vs}]$	12.95	5.562	6.034	2.815	5.101	5.082	3.270	3.261
GM	[dB]	**45**	**45**	**50**	**50**	48.8$^{\oplus}$	44.4$^{\oplus}$	51.8$^{\oplus}$	47.1$^{\oplus}$
PM	[°]	**60**	**80**	**60**	**80**	68.8$^{\oplus}$	83.8$^{\oplus}$	69.6$^{\oplus}$	85.6$^{\oplus}$
M_S		1.0570	1.0064	1.0787	1.0047	1.0101	1.0055	1.0131	1.0049
$-\sigma$	-	35.39$^{\circledast}$	50.12$^{\circledast}$	57.80$^{\circledast}$	57.22$^{\circledast}$	70	100	54.78	77.83
ω_d	[rad/s]	103.90$^{\circledast}$	101.51$^{\circledast}$	95.70$^{\circledast}$	57.97$^{\circledast}$	71.42	0	55.89	0
ξ (29)	-	0.32 **	0.44 **	0.52 **	0.70 **	0.7	1.0	0.7	1.0
ω_n (28)	[rad/s]	109.76 *	113.21 *	111.8 *	81.45 *	100	100	78.26	78.26
δ^{dem}	[%]	-	-	-	-	**4.6**	**0**	**4.6**	**0**
$\delta^{mat,m}$	[%]	21.9	5.2	15.5	3.2	10.2	3.2	8.3	1.3
$\delta^{exp,m}$	[%]	34.3	21.2	15.0	4.5	15.5	12.4	10.1	4.4
t_r^{dem}	[ms]	-	-	-	-	**18**	**18**	**23**	**23**
$t_r^{mat,m}$	[ms]	7.7	11.1	11.8	19.7	12.9	11.4	17.9	16.8
$t_r^{exp,m}$	[ms]	16.4	15.9	16.1	22.1	16.1	16.1	20.3	19.0

* Values calculated basing directly on $t_r^{exp,m}$, (28).
** Values calculated basing directly on $\delta^{exp,m}$, (29).
$^{\circledast}$ Values calculated indirectly from measurements of $t_r^{exp,m}$ and $\delta^{exp,m}$, according to $\sigma = \xi\omega_n$ and $\omega_d = \omega_n\sqrt{1-\xi^2}$.
$^{\oplus}$ Values indicated by intersections of GM and PM trajectories projected in Fig. 13 (b) - not shown in this article for simplicity reason.

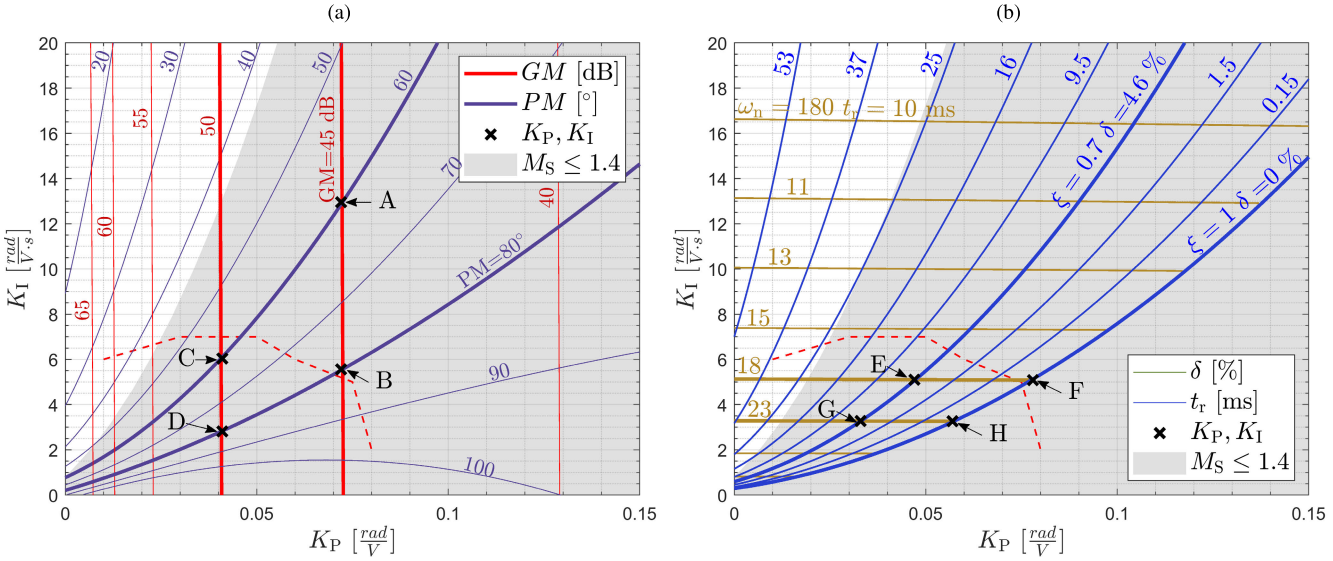

FIGURE 13. Determination of the $v_{DAB,out}$ PI controller K_P and K_I gains basing on the experimentally identified transfer function $P_{DAB}^{exp,est,c2o}(s)$ expressed by (1). Case (a) relies on the $\mathfrak{D}$-decomposition technique with constraints in the frequency domain $GM \in \{45,50\}$ dB, $PM \in \{60,80\}$ °, and case (b) is for the time domain constraints such as the overshoot $\delta \in \{0, 4.6\}$ % and the rise time $t_r \in \{18, 23\}$ ms. The grey area indicates allowable sensitivity M_S region. The dashed red line indicates the PI compensator output saturation border - this basing on observations in the experiments only.

difference between $t_r^{exp,m}$ and $t_r^{mat,m}$ is about 8.7ms for point A which represents the highest control dynamics. The difference comes from early saturation of the regulator output in the experiment during larger step commands, see the dashed lines in Fig. 13. Gains for points B and F activated the saturation too but not so aggressively because of their significantly smaller integral gains. The best match between $t_r^{exp,m}$ and $t_r^{mat,m}$ is for point D, 2.4ms absolute difference, which represents the lowest control dynamics. The difference in point D is close to the differences in points G and H, 2.4ms and 2.2ms respectively.

Further observation in terms of the rise time can be made while looking at the t_r^{dem} and $t_r^{exp,m}$ for the time domain - points E to H. It can be seen that the absolute differences are in range of 1.9..4ms. Somehow disappointing are the differences between t_r^{dem} and $t_r^{mat,m}$ which are in range of 5.1..6.2ms but again the formulas (28) and (29), used as a "translation" between the t_r, δ and ω_n, ξ respectively, are only rough approximations in case of the analysed closed-loop transfer function (2). The 1.8 value in (28) comes as an averaging compromise from second-order system step response with $\xi = 0.5$, without zero, which is different from the considered

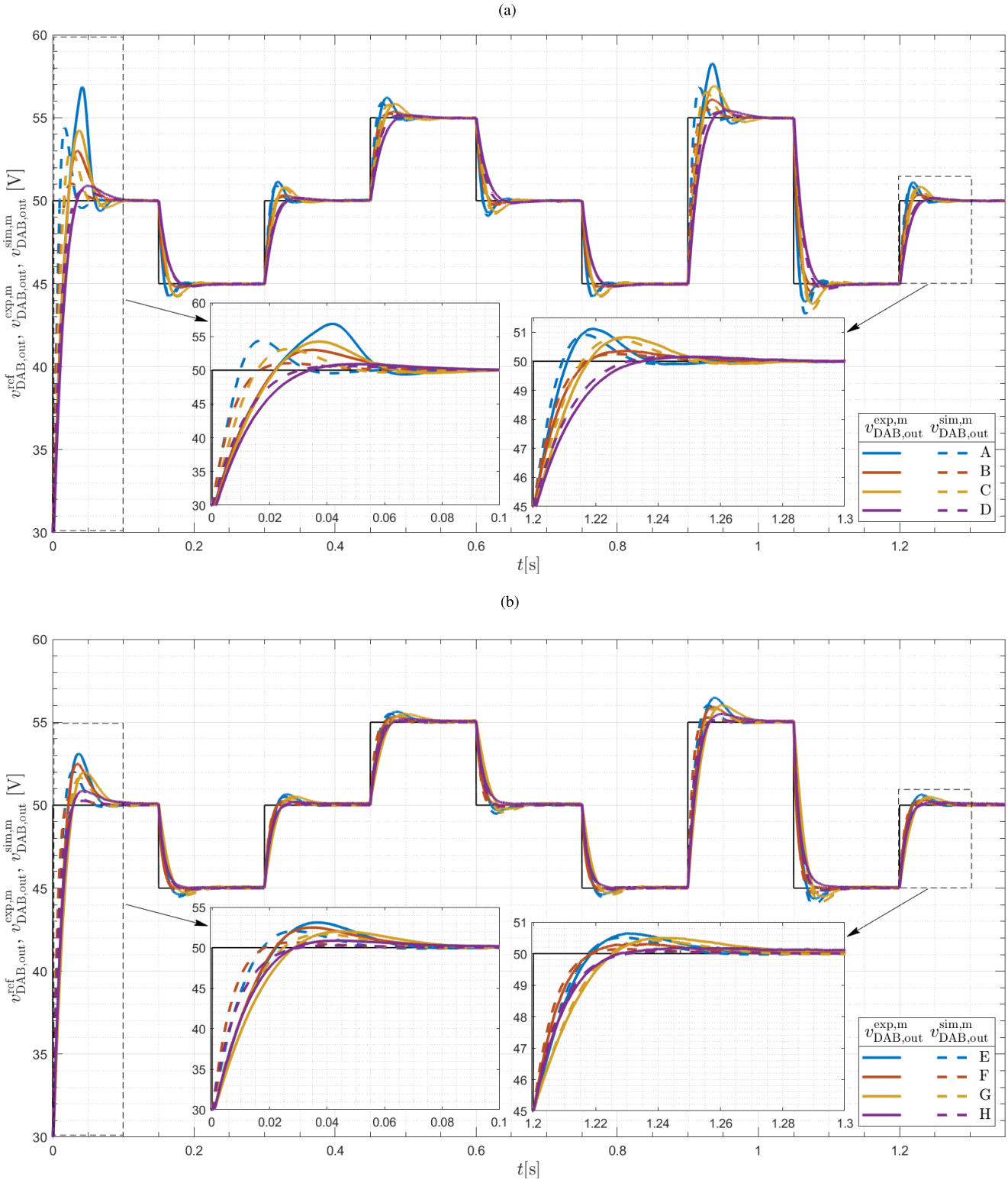

FIGURE 14. Measured DAB converter output voltage in experiment, $v^{\mathrm{exp,m}}_{\mathrm{DAB,out}}$, and in mathematical model, $v^{\mathrm{mat,m}}_{\mathrm{DAB,out}}$ with a PI controller. The PI controller gains, shown in Tab. 1, were selected using $\mathfrak{D}$-decomposition technique with constraints in: (a) the frequency domain; (b) the time domain. The results have been recorded for the reference voltage profile, $v^{\mathrm{ref}}_{\mathrm{DAB,out}}$, at the output rated power, $P^{\mathrm{rtd}}_{\mathrm{DAB,out}}$=370 W.

values of 0.7 and 1.0. This contributes to discrepancies not only between the $t_{\mathrm{r}}^{\mathrm{dem}}$ and the $t_{\mathrm{r}}^{\mathrm{mat,m}}$ but also $t_{\mathrm{r}}^{\mathrm{exp,m}}$. Although such simplification is less noxious in case of the experimental results - they are closer to the expected values.

Comparing the overshoots $\delta^{\mathrm{exp,m}}$ and $\delta^{\mathrm{mat,m}}$ in Tab. 1 without saturation one can see that there is somehow acceptable match for points C and D where 0.5% and 1.3% absolute difference appears respectively. The points E, G, H, fall in

TABLE 2. Selected K_P and K_I gains of a IP output voltage regulator of a DAB converter - this with use of Neimark's $\mathfrak{D}$-decomposition technique. Points I-L are related to the frequency domain constrains, *GM* and *PM*, see Fig. 17 (a) while points M-P come from the time domain constrains such as the rise time t_r and overshoot δ, see Fig. 17 (b). The input requirements are in bold. The table also contains associated experimentally measured and calculated parameters with annotations. Points with 'sat' subindex denote the controller output saturation during experimental tests.

Parameter	Unit	$I_{(SAT)}$	J	$K_{(SAT)}$	L	M	N	O	P
K_P	$[\frac{rad}{V}]$	0.128	0.129	0.072	0.072	0.062	0.171	0.042	0.130
K_I	$[\frac{rad}{Vs}]$	30.73	11.85	12.89	5.562	7.182	18.90	4.409	11.67
GM	[dB]	**40**	**40**	**45**	**45**	46.5$^{\oplus}$	37.5$^{\oplus}$	49.7$^{\oplus}$	40.0$^{\oplus}$
PM	[°]	**60**	**80**	**60**	**80**	68.7$^{\oplus}$	78.9$^{\oplus}$	69.1$^{\oplus}$	80.1$^{\oplus}$
M_S		1.0432	1.0053	1.0559	1.0064	1.0086	1.0023	1.0115	1.0049
$-\sigma$	-	25.64$^{\circledast}$	111.50$^{\circledast}$	37.55$^{\circledast}$	83.33$^{\circledast}$	83.13	194.46	65.10	152.19
ω_d	[rad/s]	69.73$^{\circledast}$	66.11$^{\circledast}$	74.55$^{\circledast}$	49.41$^{\circledast}$	84.81	0.0	66.40	0.0
ξ (29)	-	0.35 **	0.86 **	0.45 **	0.86 **	0.70	1.00	0.70	1.00
ω_n (30)	[rad/s]	74.30 *	129.62 *	83.78 *	96.88 *	118.8	194.46	92.94	152.19
δ^{dem}	[%]	-	-	-	-	**4.6**	**0.0**	**4.6**	**0.0**
$\delta^{mat,m}$	[%]	12.1	0.0	10.2	0.1	4.6	0.0	4.7	0.0
$\delta^{exp,m}$	[%]	31.5	0.5	20.7	0.5	7.1	0.6	5.3	0.0
t_r^{dem}	[ms]	-	-	-	-	**18.0**	**18.0**	**23.0**	**23.0**
$t_r^{mat,m}$	[ms]	7.9	21.4	11.4	27.9	17.9	17.2	22.7	22.2
$t_r^{exp,m}$	[ms]	16.2	21.6	16.7	28.9	19.7	16.9	25.0	21.9

* Values calculated basing directly on $t_r^{exp,m}$, (30).
** Values calculated basing directly on $\delta^{exp,m}$, (29).
$^{\circledast}$ Values calculated indirectly from measurements of $t_r^{exp,m}$ and $\delta^{exp,m}$, according to $\sigma = \xi\omega_n$ and $\omega_d = \omega_n\sqrt{1-\xi^2}$.
$^{\oplus}$ Values indicated by intersections of GM and PM trajectories projected in Fig. 17 (b) - not shown in this article for simplicity reason.

range of 1.8..5.3% of the difference and are less satisfactory. Points A, B and F with saturation in experiment are within 9.2..16% the difference range.

By referencing now to the δ^{dem} one can see that mathematical model results (1.3..5.6% differences range) are generally closer to the demanded values when compared to experimental 4.4..10.9% differences range. Despite of no saturation in the mathematical model the results do not match satisfactory the demands - this is mainly due to the closed loop transfer function zero effect.

Nevertheless the estimated (by simple means of step response analysis) $1^{st}-$order plant transfer function is good enough for general purpose PI compensator gains selection with the $\mathfrak{D}$-decomposition technique. Both methods, in the frequency and in the time domain, lead to stable overall closed-loop control performance with the M_S slightly above 1. However benefits from additional calculations according to (28) (29) are not obvious when compared to the *GM* and *PM* criteria. The measured rise times and overshoots are not close enough to demanded values.

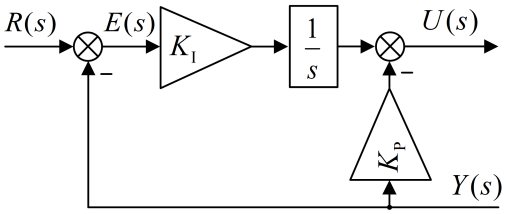

FIGURE 15. The IP configuration of a PI compensator.

B. THE IP CONFIGURATION OF THE PI COMPENSATOR

The IP configuration shown in Fig. 15 has been tested. It is known for its zero-compensating properties - this of course on

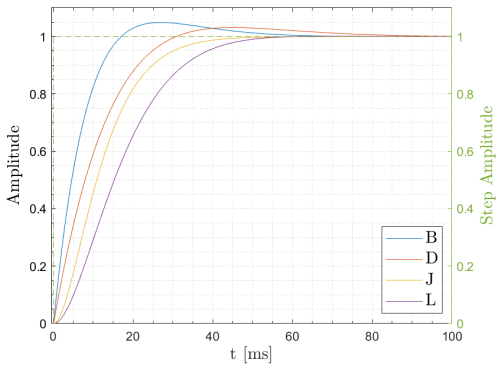

FIGURE 16. Comparison of the step responses with the PI and the IP compensators configurations with settings according to points B and D in Tab. 1, and points J and L in Tab. 2.

TABLE 3. Parameters of the DAB circuit.

Parameter Name	Value
Input rated voltage, $V_{DAB,in}^{rtd}$	100 VDC
Output rated voltage, $V_{DAB,out}^{rtd}$	50 VDC
Output rated power, $P_{DAB,out}^{rtd}$	370 W
Output voltage tolerance, $V_{DAB,out}^{tol}$	±10 %
Converter inductance, L	140 μH
DAB input capacitance, $C_{DAB,in}$	4 mF
DAB output capacitance, $C_{DAB,out}$	3.3 mF
Transformer turn ratio, n	2
Switching frequency, f_s	16 kHz
DAB assumed efficiency, η_{DAB}	85 %
Gate drive dead time, T_{dt}	1 μs

an expense of reduced response dynamics with gains identical to the PI configuration.

Assuming sufficient compensation of the zero, more accurate formula for the ω_n could be used instead of (28):

$$\omega_n = \frac{1 - 0.4167\xi + 2.917\xi^2}{t_r} \tag{30}$$

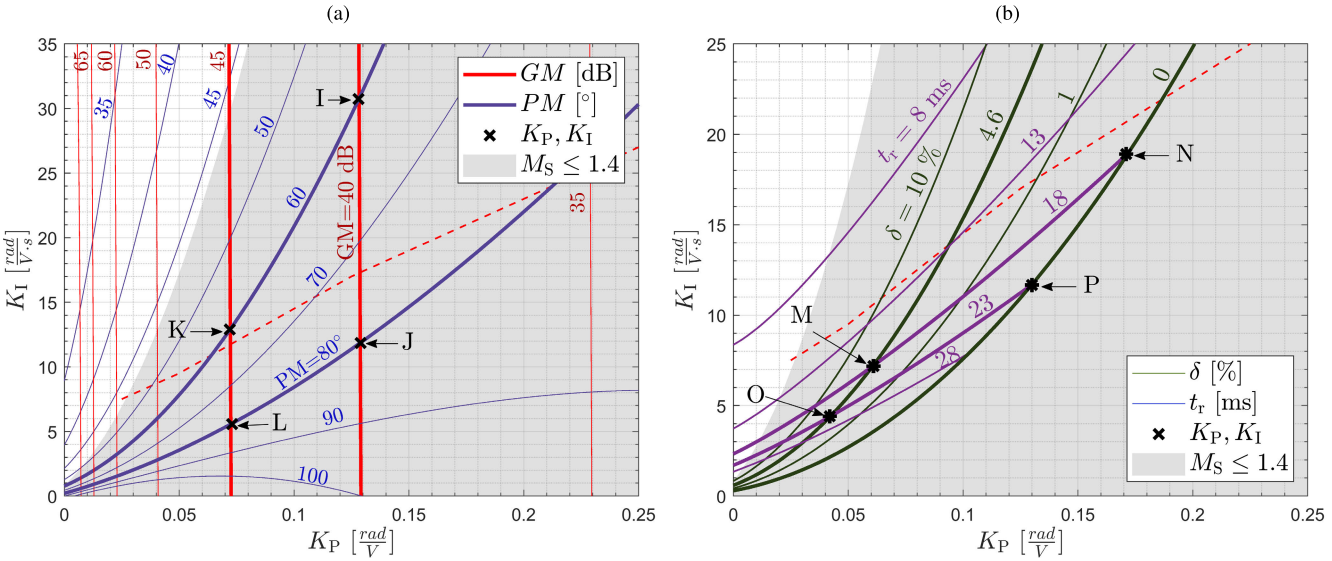

FIGURE 17. Determination of the $v_{DAB,out}$ IP controller K_P and K_I gains basing on the experimentally identified transfer function $P_{DAB}^{exp,est,c2o}(s)$ expressed by (1). Case (a) relies on the $\mathfrak{D}$-decomposition technique with constraints in the frequency domain, $GM \in \{40, 45\}$ dB, $PM \in \{60, 80\}$ °, and case (b) is for the time domain constraints such as the overshoot $\delta \in \{0, 4.6\}$ % and the rise time $t_r \in \{18, 23\}$ ms. The grey area indicates allowable sensitivity M_S region. The dashed red line indicates the IP compensator output saturation border - this basing on observations in the experiments only.

The K_P and K_I gains were selected in the same manner as in case of the standard PI configuration described in section III-B - the equations (16)..(19) were used. Nevertheless the GM range as one of the two design constrains in the frequency domain has been shifted down by 5dB. Instead of $GM = \langle 45, 50 \rangle$dB, $GM = \langle 40, 45 \rangle$dB has been used - this with unchanged $PM = \langle 60, 80 \rangle°$. Such change was introduced to accelerate the voltage response in absence of the zero effect. Comparison of step responses with the two GM ranges can be seen in Fig. 16. Criterion of about zero overshoot, $\delta^{mat,m} \approx 0\%$, at the smallest rise time, $t_r^{mat,m}$, was used for the lower GM range selection. Obtained sets of gains are named as points I, J, K and L, see Fig. 17 (a).

In the time domain $t_r^{dem} = \langle 18, 23 \rangle$ms and $\delta^{dem} = \langle 0, 4.6 \rangle\%$ led to four values of ω_n according to (30) - this with the $\xi = \langle 0.7, 1 \rangle$ calculated with (29). They were designated as points M, N, O and P shown in Fig. 17 (b).

All the obtained gains together with additionally calculated and measured values can be seen in Tab. 2. All of them satisfy the sensitivity criterion with the M_S slightly bigger than one. Complete set of the output voltage responses in time can be seen in Fig. 18. Test conditions were the same as for the standard PI configuration results shown in Fig. 14.

All the plots from Fig. 18 indicate stable converter operation. The mathematical results, $t_r^{mat,m}$ and $\delta^{mat,m}$, are in closer accordance with the experimental results, $t_r^{exp,m}$ and $\delta^{exp,m}$, than in case of the PI. Exceptions are the points I and K. In these two points saturation of the IP compensator output took place during the $20V$ and $10V$ up-steps. This contributed to 8.3ms, 19.4% and 5.3ms, 10.5% absolute differences respectively. Remaining points (J, L, . . . , P) are within absolute difference ranges of 0.2..2.3ms for the rise times and 0..2.5% for overshoots. Here it is worth to notice that the rise times, both $t_r^{mat,m}$ and $t_r^{exp,m}$, of points L, M, O, P are longer than their PI equivalents in points D, E, G, H respectively. This is a side effect of the zero compensation in this standard control structure.

The absolute differences between the demanded values, t_r^{dem} and δ^{dem} and the measured ones in points M, N, O, P are in ranges: 0.1..0.8ms and 0..0.1% for the mathematical model, 1.1..2ms and 0..2.5% for the experimental circuit. Still existing differences between the δ^{dem}, t_r^{dem} and $\delta^{mat,m}$, $t_r^{mat,m}$ are driven by the fact that formulas (28) and (30) are still only averaging solutions. Bigger differences in case of $\delta^{exp,m}$, $t_r^{exp,m}$ are driven by high frequency compromises in the identified control-to-output transfer function (1).

In terms of general summary about the IP configuration one can say that there is considerable correlation between the time domain demanded values and their measured equivalents. It is true for the mathematical model and for the experiment. Absolute differences in results of the experimental IP and the corresponding PI are within following ranges: 1.1..2ms vs. 1.9..4ms for the rise times, 0..2.5% vs. 4.4..10.9% for the overshoots. In case of the mathematical IP vs. PI the absolute difference ranges are: 0.1..0.8ms vs. 5.2..6.2ms for the rise times, 0..0.1% vs. 1.3..5.6% for the overshoots. It is worth to notice that there is a good match between the mathematical model and experimental results. This from one side confirms the mathematical apparatus used and form the other side helps to understand subtle compromises made at the time domain criterion facilitation stage. All that in relation to an identified transfer function.

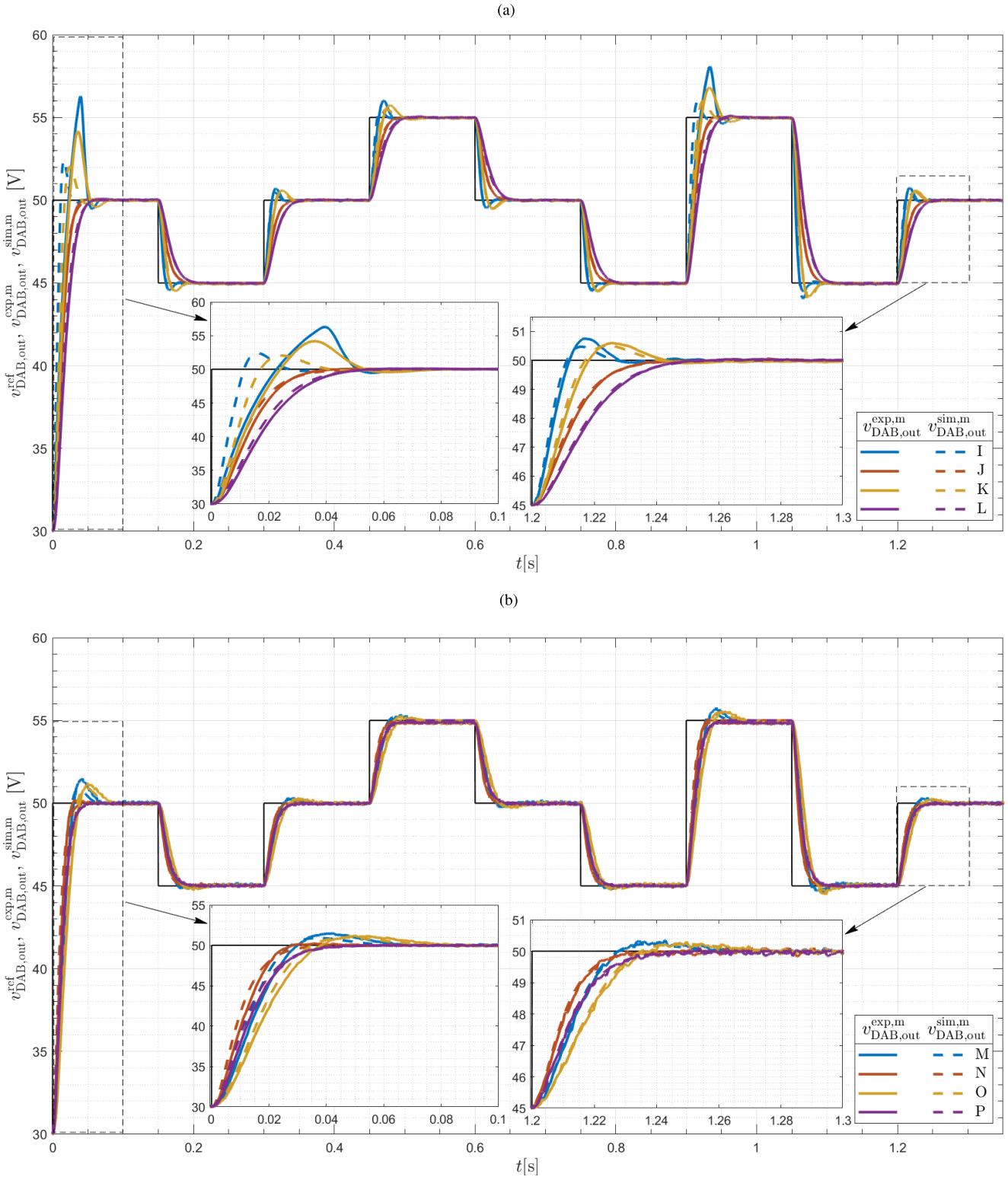

FIGURE 18. Measured DAB converter output voltage in experiment, $v^{\mathrm{exp,m}}_{\mathrm{DAB,out}}$, and in mathematical model, $v^{\mathrm{mat,m}}_{\mathrm{DAB,out}}$ with IP controller configuration shown in Fig. 15. The IP controller gains, shown in Tab. 2, were selected using $\mathfrak{D}$-decomposition technique with constraints in: (a) the frequency domain; (b) the time domain. The results have been recorded for the reference voltage profile, $v^{\mathrm{ref}}_{\mathrm{DAB,out}}$, at the output rated power, $P^{\mathrm{rtd}}_{\mathrm{DAB,out}} = 370$ W.

V. CONCLUSION

Practical variants of the PI- and IP-type compensator gains selection by means of the $\mathfrak{D}$-decomposition technique are presented in this paper. The content relies on systematic and intelligible approach to mathematical analysis verified experimentally. All is based on a closed loop DAB converter

output voltage regulation example. The circuit operates under the phase shift control scheme. Practical aspects of the control design such as the control-to-output transfer function identification and the control delays are sufficiently addressed too.

Commonly used the frequency- and the time-domain driven requirements regarding the control dynamics have been combined with the $\mathfrak{D}$-decomposition technique. This has contributed to creation of a consistent picture of possible paths leading to fulfillment of the control requirements.

The investigated paths, as a matter of a designer preference, lead through: (i.) the GM, PM and the M_S specification in the frequency domain, (ii.) the time domain indirectly by the pole placements with the (σ, ω_d) or (ξ, ω_n) specification, (iii.) the time domain directly by approximate relations between the (ξ, ω_n) and the (σ, t_r). These somewhat advanced techniques have been reduced by the means of the $\mathfrak{D}$-decomposition to rather simple design tasks relying on judgments in the intuitive (K_P, K_I) gains coordinates with relevant parametric curves added.

Conducted analyses have revealed that for the given control case the direct time domain requirements are less effectively met with the PI regulator when compared to its IP configuration. This is due to compromises related to the transitions between the (ξ, ω_n) and the (σ, t_r) in presence of the closed loop transfer function uncompensated zero. Therefore the IP configuration is recommended for cases when the time domain direct requirements are used. Here one should be aware of reduced dynamic performance. This is a price paid for the zero effect reduction with this basic control scheme.

In the era of numerical computing the $\mathfrak{D}$-decomposition technique, originally used for the stability boundary indication only, combined with additional control criteria can constitute for very effective and at the same intuitive means of control design with the PI-type regulators. The mathematical apparatus can also be extended to the PID controllers by introducing an additional parameter.

ACKNOWLEDGMENT

The authors would like to thank Dr. Marcin Zygmanowski for inspiring discussions in the field of practical power electronics.

REFERENCES

[1] K. J. Aström, T. Hägglund, and K. J. Astrom, *Advanced PID Control*, vol. 461. Gurugram, China: ISA, 2006.
[2] K. Ogata, *Modern Control Engineering*. Upper Saddle River, NJ, USA: Prentice-Hall, 2010.
[3] R. W. Erickson and D. Maksimovic, *Fundamentals Power Electronics*. Norwell, MA, USA: Kluwer, 2007.
[4] B. Kristiansson and B. Lennartson, "Robust tuning of PI and PID controllers: Using derivative action despite sensor noise," *IEEE Control Syst.*, vol. 26, no. 1, pp. 55–69, Feb. 2006.
[5] Y. Li, K. H. Ang, and G. C. Y. Chong, "PID control system analysis and design," *IEEE Control Syst.*, vol. 26, no. 1, pp. 32–41, Feb. 2006.
[6] J. Niejmark, "Ob opriedielenji znaczenij paramietrow, pri kotorych sistiema awtomaticzeskogo riegulirowanja ustojczziwa," *Awtomatika Telemiechanika*, vol. 3, pp. 193–200, Oct. 1948.
[7] Z. Shafiei and A. T. Shenton, "Relative stability for open-loop stable and unstable discrete control systems with perturbed or adjustable parameters," in *Proc. Eur. Control Conf. (ECC)*, Aug. 1999, pp. 2180–2185.
[8] J. Ackermann, "Hurwitz-stability boundary crossing and parameter space approach," in *Robust Control*. London, U.K.: Springer-Verlag, 2002, pp. 29–58.
[9] S. Han and S. Bhattacharyya, "PID controller synthesis using σ-hurwitz stability criterion," *IEEE Control Syst. Lett.*, vol. 2, no. 3, pp. 525–530, Jun. 2018.
[10] K. Najdek and R. Nalepa, "Use of the d-decomposition technique for gains selection of the dual active bridge converter output voltage regulator," *Przegląd Elektrotechniczny*, vol. 95, pp. 268–273, Dec. 2019.
[11] C.-H. Chang and K.-W. Han, "Gain margins and phase margins for control systems with adjustable parameters," *J. Guid., Control, Dyn.*, vol. 13, no. 3, pp. 404–408, May 1990.
[12] S. M. Tripathi, A. N. Tiwari, and D. Singh, "Controller design for a variable-speed direct-drive permanent magnet synchronous generator-based grid-interfaced wind energy conversion system using d-partition technique," *IEEE Access*, vol. 5, pp. 27297–27310, 2017.
[13] X. Liao, Y. Wang, and L. Dong, "Maximum sensitivity based fractional-order controller for permanent magnet synchronous motor system with time delay," in *Proc. IEEE Int. Conf. Syst., Man, Cybern. (SMC)*, Oct. 2017, pp. 2267–2272.
[14] P. Li, P. Wang, and X. Du, "An approach to optimal design of stabilizing PID controllers for time-delay systems," in *Proc. Chin. Control Decis. Conf.*, Jun. 2009, pp. 3465–3470.
[15] B. Shen, Q. Zhao, L. Ou, and G. Li, "Design of h_∞ three-delay controllers for systems with time delay," in *2014 Int. Conf. Mechatronics Control (ICMC)*, Jul. 2014, pp. 1432–1437.
[16] H. Li, X. Zhang, S. Yang, E. Li, and J. Hong, "Multi-objective controller design of IPMSM drives based on DTD D-partition method considering parameters uncertainties," *IEEE Trans. Energy Convers.*, vol. 34, no. 2, pp. 1052–1062, Jun. 2019.
[17] R. W. A. A. De Doncker, D. M. Divan, and M. H. Kheraluwala, "A three-phase soft-switched high-power-density DC/DC converter for high-power applications," *IEEE Trans. Ind. Appl.*, vol. 27, no. 1, pp. 63–73, Jan. 1991.
[18] I. Kayaalp, T. Demirdelen, T. Koroglu, M. U. Cuma, K. C. Bayindir, and M. Tumay, "Comparison of different phase-shift control methods at isolated bidirectional dc-dc converter," *Int. J. Appl. Math. Electron. Comput.*, vol. 4, no. 3, pp. 68–73, 2016.
[19] L. Shi, W. Lei, J. Huang, Z. Li, Y. Cui, and Y. Wang, "Full discrete-time modeling and stability analysis of the digital controlled dual active bridge converter," in *Proc. IEEE 8th Int. Power Electron. Motion Control Conf. (IPEMC-ECCE Asia)*, May 2016, pp. 3813–3817.
[20] T. L. Nguyen, G. Griepentrog, and V. T. Phung, "Modeling and control of dual active bridge converter with two control loops and output filter," in *Proc. 43rd Annu. Conf. Ind. Electron. Soc.*, Oct. 2017, pp. 4683–4689.
[21] R. Nalepa, M. Zygmanowski, and J. Michalak, "Dual-active-bridge converter inductance dc-bias current compensation under low and high load conditions," *Organ*, vol. 7, p. 18, Oct. 2018.
[22] Y. I. Neimark, "Determination of the values of parameters for which an automatic system is stable," *Avtomat. Telemekh*, vol. 9, pp. 190–203, May 1948.
[23] A. T. Shenton and Z. Shafiei, "Relative stability for control systems with adjustable parameters," *J. Guid., Control, Dyn.*, vol. 17, no. 2, pp. 304–310, Mar. 1994.
[24] N. Sayyaf and M. S. Tavazoei, "Frequency data-based procedure to adjust gain and phase margins and guarantee the uniqueness of crossover frequencies," *IEEE Trans. Ind. Electron.*, vol. 67, no. 3, pp. 2176–2185, Mar. 2020.
[25] S. S. Mikhalevich, S. A. Baydali, and F. Manenti, "Development of a tunable method for PID controllers to achieve the desired phase margin," *J. Process Control*, vol. 25, pp. 28–34, Jan. 2015.
[26] S. Chakraborty, S. Ghosh, and A. K. Naskar, "All-PD control of pure integrating plus time-delay processes with gain and phase-margin specifications," *ISA Trans.*, vol. 68, pp. 203–211, May 2017.
[27] J. Osuskỳ and V. Veselỳ, "Modification of neimark d-partition method for desired phase margin," in *Proc. Int. Conf.*, vol. 10, 2010, p. 13.
[28] H. Panagopoulos, T. Hägglund, and K. J. Åström, "Design of PID controllers based on constrained optimisation," *IEE Proc.-Control Theory Appl.*, vol. 149, no. 1, pp. 32–40, Jan. 2002.
[29] J. Ackermann, *Robust Control: Parameter Space Approach*. London, U.K.: Springer-Verlag, 2002.
[30] P. Mercader, K. J. Astrom, A. Banos, and T. Hagglund, "Robust PID design based on QFT and convex–concave optimization," *IEEE Trans. Control Syst. Technol.*, vol. 25, no. 2, pp. 441–452, Mar. 2017.

[31] R. Villafuerte-Segura, F. Medina-Dorantes, L. Vite-Hernández, and B. Aguirre-Hernández, "Tuning of a time-delayed controller for a general class of second-order linear time invariant systems with dea-time," *IET Control Theory Appl.*, vol. 13, no. 3, pp. 451–457, Feb. 2019.
[32] G. F. Franklin, J. D. Powell, A. Emami-Naeini, and H. Sanjay, *Feedback Control of Dynamic Systems*. London, U.K.: Pearson, 2015.
[33] M. F. G. B. C. Kuo, *Automatic Control Systems*. New York, NY, USA: McGraw-Hill, 2017.
[34] I. H. Kim and Y. I. Son, "Regulation of a DC/DC boost converter under parametric uncertainty and input voltage variation using nested reduced-order PI observers," *IEEE Trans. Ind. Electron.*, vol. 64, no. 1, pp. 552–562, Jan. 2017.
[35] R. Nalepa, K. Najdek, K. Wróbel, and K. Szabat, "Application of D-decomposition technique to selection of controller parameters for a two-mass drive system," *Energies*, vol. 13, no. 24, p. 6614, Dec. 2020.

KAROL NAJDEK received the M.Sc. degree in electrical engineering from the Wrocław University of Science and Technology, Wrocław, Poland, in 2017, where he is currently pursuing the Ph.D. degree.

He is also working as an Assistant with the Department of Electrical Power Engineering, Division of Power Networks and Systems, Wrocław University of Science and Technology. His research interests include power converters and power electronics systems and control.

RADOSLAW NALEPA received the M.Sc. degree in electrical engineering from the Wrocław University of Science and Technology, Wrocław, Poland, in 1997, and the Ph.D. degree in control of switch mode power supplies from the Cork Institute of Technology, Cork, Ireland, in 2001.

From 2001 to 2006, he was with Moog Ltd., Cork, working as a Research and Development Engineer for PMSM motor drives. From 2006 to 2009, he was with Moog GmbH, Boeblingen, Germany, working as a research and development engineer and the leader of projects related to multi-axis AC/AC and DC/AC drives development. From 2009 to 2011, he was with the Institute of Electrical Machines, Drives and Measurements, Wrocław University of Science and Technology, as an Assistant Professor. From 2011 to 2013, he was with the ABB Corporate Research Center, Poland, as a Power Electronics Principal Scientist and the Project Manager. From 2013 to 2016, he was with the KGHM Polska Miedz S.A., Poland, as the Chief Specialist and the Automation Commissioning Manager deputy during a new głogów copper smelter construction and launching. Since February 2017, he has been with the Faculty of Electrical Engineering, Wrocław University of Science and Technology, as an Assistant Professor, working on power electronics and control.